Structural and electrochemical Investigation of $Li(Ni_{0.4}Co_{0.2-y}Al_yMn_{0.4})O_2$ Cathode Material

C. Rumble[a], T. E. Conry[b], Marca Doeff[b], Elton J. Cairns[c, d], James E. Penner-Hahn[a], Aniruddha Deb[a,1]

[a] Department of Chemistry, University of Michigan, Ann Arbor, MI 48109, USA

[b] Materials Science Division, Lawrence Berkeley National Laboratory, Berkeley, CA 94720, USA

[c] Environmental Energy Technologies Division, Lawrence Berkeley National Laboratory, Berkeley, CA 94720, USA

[d] Department of Chemical Engineering, University of California, Berkeley, CA 94720, USA

[1] E-mail: debani@umich.edu

Abstract

$Li(Ni_{0.4}Co_{0.2-y}Al_yMn_{0.4})O_2$ with y=0.05 was investigated to understand the effect of replacement of the cobalt by aluminum on the structural and electrochemical properties. The effect of the substitution was studied by *in-situ* X-ray absorption spectroscopy (XAS), utilizing a novel *in situ* electrochemical cell, specifically designed for long-term X-ray experiments. The cell was cycled at a moderate rate through a typical Li-ion battery operating voltage range (1.0–4.7 V). XAS measurements were performed at different states-of-charge (SOC) during cycling, at the Ni, Co, and the Mn edges, revealing details about the response of the cathode to Li insertion and extraction processes. The extended X-ray absorption fine structure region of the spectra revealed the changes of bond distance and coordination number of Ni, Co, and Mn absorbers as a function of the SOC of the material. The oxidation states of the transition metals in the system are Ni^{2+}, Co^{3+}, and Mn^{4+} in the as-made material (fully discharged), while during charging the Ni^{2+} is oxidized to Ni^{4+} through an intermediate stage of Ni^{3+}, Co^{3+} is oxidized towards Co^{4+} and Mn was found to be electrochemically inactive and remains as Mn^{4+}. The EXAFS results during cycling show that the Ni-O changes the most, followed by Co-O and Mn-O varies the least. These measurements on this cathode material confirmed that the material retains its symmetry and good structural short-range order leading to the superior cycling reported earlier.

Introduction

Environmentally friendly and economical lithium battery electrode materials with higher capacity and good cycling stability are in high demand. With the emergence of portable telecommunications, computer equipment, and, ultimately, hybrid electric vehicles, there has been a great demand for less expensive batteries with longer life times and smaller sizes and weights. $LiCoO_2$ has been the backbone for commercial use in Li-ion batteries since their inception by Sony, due to its ease of production, stable electrochemical cycling, and acceptable specific capacity. The relatively high cost and toxicity of cobalt, and the quest for materials with higher capacities have led to the study of possible alternatives, though many have limitations precluding their widespread use. $LiNiO_2$ is thermally unstable at high states-of-charge.[1] Variants of $LiMn_2O_4$ exhibit good structural stability on overcharge but have low capacity, and exhibit high solubility of Mn^{2+} in the electrolyte at elevated temperatures above 55 °C.[2] Layered systems like $LiNi_{0.8}Co_{0.15}Al_{0.05}O_2$ have attracted attention as a cathode for lithium-ion batteries especially for hybrid electric vehicle applications.[2] Compared to $LiCoO_2$, this system proved to possesses enhanced electrochemical performance at a projected lower cost.[3] Other layered materials under consideration as cathode materials for Li ion batteries include NMCs, which have the general formula $Li[Ni_xCo_{1-2x}Mn_x]O_2$[3]; where x is most commonly equal to 1/3. There have recently been attempts to further reduce the Co content (for example, $Li[Ni_{0.4}Co_{0.2}Mn_{0.4}]O_2$)[4]. This has met with some success, but rate capability of the electrodes tends to decrease as the Ni content is raised due to increased anti-site mixing. Clearly there is a great deal of interest, however, in the synthesis and characterization of layered compounds with reduced Co content.[4-7]

Recently, $Li(Ni_{1/3}Co_{1/3-y}Al_yMn_{1/3})O_2$; $0 \leq y \leq 1/3$[8] and $Li(Ni_{0.4}Co_{0.2-y}Al_yMn_{0.4})O_2$; $0 \leq y \leq 0.2$[9] compounds were studied as cathode materials. For low values of y, aluminum substitution appears to improve the rate capability and cycling stability compared to the baseline materials. Other studies on Al substitution of layered oxide structures suggest that the thermal abuse tolerance is improved.[10, 11] These results motivated us to investigate specific Al-substituted materials using *in-situ* X-ray absorption spectroscopy (XAS) to elucidate the implications of substitution of Co for Al. An ultimate goal is to allow design of low Co content layered oxides with improved electrochemical properties.

There has been a continuous effort to study the detailed changes that occur in various electrode materials during the charge-discharge process. Real-time tracking of the structure and valence changes during delithiation, relithiation and prolonged cycling of layered cathode materials may have predictive value for determining the intrinsic electrochemical characteristics, and can be achieved by employing an *in-situ* electrochemical cell. X-ray absorption spectroscopy (XAS), accompanied by simultaneous electrochemical measurements, provide valuable and important information about the relationship between the structure and electrochemical properties of the electrode materials, information that is not always accessible utilizing *ex-situ* experimental measurements.

In this investigation, we present a comprehensive transmission XAS study to investigate $Li(Ni_{0.4}Co_{0.2-y}Al_yMn_{0.4})O_2$ (y=0.05) electrodes (as used in Li-ion batteries) at various states of charge. Information about the oxidation state of the investigated transition metal elements (in this case, Mn, Co, and Ni) and their electronic configuration was obtained from the X-ray absorption near-edge spectroscopy (XANES) region of the

K-absorption edges, whereas the extended X-ray absorption fine structure (EXAFS) region was used to probe the structure around the X-ray absorbing atoms.

Experimental Procedures

$Li(Ni_{0.4}Co_{0.15}Al_{0.05}Mn_{0.4})O_2$ powder was synthesized and electrodes prepared as previously described.[9] The specifications of the electrode are given in Table I. Phase purity was assessed by x-ray powder diffraction (XRD) using a Phillips X'Pert diffractometer with an X'celerator detector and Cu Kα radiation. The experiments were performed using a complete $Li/Li(Ni_{0.4}Co_{0.15}Al_{0.05}Mn_{0.4})O_2$ half-cell. A special electrochemical *in-situ* XAS cell was used for these experimental investigations; for a complete detailed design and assembly the reader is referred to Deb et al.[12] A sheet of porous polypropylene membrane (Celgard 3400) was utilized as a separator and 1 M $LiPF_6$ in ethylene carbonate (EC)+diethyl carbonate (DEC) (1:1 volume, Merck, LP40) as the electrolyte. A Li metal foil cut into a circular disk (diameter 1.5 cm) was used as the counter electrode. The charge-discharge cycling was performed at room temperature at the beam line with a potentiostat/galvanostat system (Princeton Applied Research, Model Versa) under constant current control. *In-situ* XAS measurements performed during charging and discharging were carried out at various states of charge of the electrode. Charging and discharging were performed at a constant current density of 0.10 mA/cm^2 between 1.0 and 4.7 V, which corresponds to about the C/25 rate, assuming all of the Li could be extracted. The measurements performed at different points along the charging cycle are labeled in Fig.1. The charging was paused during the XAS measurements to allow the electrode systems to stabilize. The spectra presented here

were obtained during the charging process at different states of charge (to 4.7 V vs Li). For the measurements with the model compounds shown here for comparison, the samples were diluted with boron nitride (BN) (samples were mixed in a 1:10 ratio with BN using a mortar and pestle), and 0.8 cm^2 pellets were prepared. The sample pellets were then finally loaded on aluminum holders using Kapton adhesive foil on both sides of the sample.

The XAS measurements were performed in the transmission mode at the bending magnet beamline station D of the DND-CAT (Sector 5), at the Advanced Photon Source, using a water cooled Si(111) double crystal monochromator and the energy resolution of the monochromatic beam was determined to be ~1.0 eV. A beam size of about 0.3 x 0.5 mm^2 was used for the beam to pass easily through the in-situ cell x-ray window resulting in an incident photon flux of ~10^{10} photons/ s. For both Mn and Ni K absorption edges, the monochromator was scanned from 200 eV below to 800 eV above the K absorption edge, while the Co K-absorption edge data range was limited to a maximum of 8250 eV (12.7 $Å^{-1}$) at the onset of the Ni K edge. The EXAFS data presented were analyzed using a combination of EXAFSPAK software package[13] and Athena.[14] The resulting $\chi(k)$ function was weighted with k^3 to account for the damping of oscillations with increasing k. The radial structure functions presented here were obtained by Fourier transformation of $k^3\chi(k)$ using a k range of 1.5–16.2 $Å^{-1}$ for Mn and Ni and 1.5–12.7 $Å^{-1}$ for Co.

Results and Discussion

$Li(Ni_{0.4}Co_{0.2-y}Al_yMn_{0.4})O_2$ ($0 \leq y \leq 0.2$) crystallizes in the R-3m space group and exhibits a well defined α-$NaFeO_2$ structure as does the parent material

$Li(Ni_{0.4}Co_{0.2}Mn_{0.4})O_2$ [9]. Al-substitution causes the **a** unit cell parameter to decrease by 0.1% and the **c** unit cell parameter to increase by 0.2% compared to the parent material. There is also an increase in the degree of anti-site mixing (Ni in the 3a or lithium sites) from 6.6 to 7.3% and a slight increase in the lithium slab spacing, which results in improved lamellarity upon substitution with Al.

In general, the shape of the K-edge XANES of the transition metal oxides provides unique information about the site symmetry and the nature of the bonding with surrounding ligands, while the threshold energy position of the absorption edge provides information about the oxidation state of the probed atom. To extract the information of the initial oxidation state of the transition metals in this material and elucidate the charge compensation mechanism in this system, Mn, Co, and Ni K-edge XAS experiments were carried out during the charge/discharge cycle at a constant current density of 0.1 mA/cm^2. The specific capacity was calculated from the elapsed time, current, and the mass of the active material in the cathode, assuming that all the current passed was due to the Li deintercalation. The comparison of the XANES region before charging [x = 1.0 (point A) in Fig.1] with that of the model compounds is shown in Fig. 2. The comparison [Fig.2(a)] reveals that the edge energy is essentially the same as that of MnO_2 (Mn^{4+}), indicating that the oxidation state of Mn in this material at the start of the charging cycle (x = 1.0) is nearly all tetravalent (Mn^{4+}). Fig. 2(b), indicates that the XANES spectrum for the Co K edge of the sample is identical to that of $LiCoO_2$ (Co^{3+}), indicating that Co in the sample at the beginning of the charging is Co^{3+}. Fig. 2(c) shows the Ni K-edge XANES spectrum with those of the model compounds of Nickel (II) oxide (Ni^{2+}) and layered $LiNi_{0.8}Co_{0.2}O_2$ (Ni^{3+}). At x = 1.0, the XANES is similar to that of the Nickel (II) oxide, indicating that

the Ni in this system is divalent (Ni^{2+}) whereas the XANES spectrum of the layered $LiNi_{0.8}Co_{0.2}O_2$ is similar to that observed at x = 0.55, confirming that Ni is in the trivalent state (Ni^{3+}) at x = 0.55.

XANES spectra for selected points during the charging process for Mn, Co, and Ni edges are shown in Fig. 3. For the Mn K-edge XANES [Fig. 3(a)], during charge, the edge position of the scans at different states of charge did not exhibit any significant edge shift to higher energies, though they do exhibit some changes in regards to the shape of the edge due to the change in the local environment of the Mn in the system as Li is deintercalated. The edge does not exhibit any rigid shift to higher energies, however, suggesting that the Mn oxidation state remains unchanged during the charging procedure, i.e., the Mn^{4+} atom is electrochemically inactive. The Co K edge [Fig. 3(b)] shows a progression of the entire pattern from lower energy to higher energy as a function of the decreased Li content (at the different charge states), indicating the oxidation of Co^{3+} towards Co^{4+}.

XANES spectra for the Ni K-edge shown in Fig. 3(c), indicate that the Ni ion undergoes a two-stage change during the charging cycle, where the first stage ranges from x = 1.0 to x = 0.55 and the second stage is from x = 0.55 to x = 0.19. Beyond x = 0.23 (Fig. 4), the Ni K edge XANES did not move significantly to a higher energy. This two-stage reaction observation may be attributed to the two one-electron reactions of the Ni ions (Ni^{2+}/Ni^{3+} and Ni^{3+}/Ni^{4+}) during charging. Similar observations of the redox reaction have been reported previously by Koyama et al. [15] using *ab-initio* calculations, for $Li_{1-x}Ni_{1/3}Co_{1/3}Mn_{1/3}O_2$ consisting of Ni^{2+}/Ni^{3+}, Ni^{3+}/Ni^{4+}, and Co^{3+}/Co^{4+}, in the ranges of $0 \leq x \leq 1/3$, $1/3 \leq x \leq 2/3$, and $2/3 \leq x \leq 1$, respectively. During discharge, these

processes are reversed electrochemically: Li is inserted in the lattice, Co^{4+} is reduced to Co^{3+}, Ni^{4+} is reduced to Ni^{2+} and M–O (metal-oxygen) and M–M (metal-metal) bond lengths return to their original values. For the purposes of this discussion, the results during charge will be discussed hereafter.

To make sure of the presence of the Ni^{3+} species at x = 0.55, we see that the absorption edges for Ni in the various states of charge cannot be represented by linear combinations of only Ni^{4+} and Ni^{2+} spectra. Fig. 3(d) shows a comparison of the spectrum calculated as a linear combination of the two species of Ni^{2+} and Ni^{4+} spectra and the spectrum for x = 0.55. The important areas of mismatch are the region near 8352 eV (just before the absorption maximum), the absorption maximum and regions near 8358 eV and 8363 eV (after the absorption maximum). The mismatch in the absorption maximum is an indication of the presence of Ni^{3+} instead of a combination of Ni^{2+} and Ni^{4+}. This evidence indicates that Ni^{3+} is an intermediate state for the Ni during oxidation/reduction cycling.

The pre-edge peaks of the respective XAS spectra are also shown in Fig. 3. These give additional information on the nature of the electronic states. For most transition metal elements, the pre-edge peaks that occur well below the main edge (~15 eV below) are assigned to transitions to empty states with d-like character [$1s \rightarrow 3d^{(n+1)}$] transitions,[16, 17] where n represents the initial number of d electrons and (n+1) includes the excited electron in the final state, which includes the effect of the core hole. These $1s \rightarrow 3d$ transitions are directly allowed through a very weak quadrupole transition [18] or allowed via an admixture of 3d and 4p states. [19] The weak pre-edge in the Mn-absorption (Fig. 3a, peaks A and A' near 6542 and 6544 eV), is the formally electric dipole-forbidden

transition of a 1s electron to an unoccupied 3d orbital of a high spin ($t_{2g}^3 e_g^0$) Mn^{4+} ion. which is partially allowed because of the pure electric quadrupole coupling and/or the 3d-4p (or Mn 3d–O 2p) orbital mixing. The presence of weak pre-edge intensity is indicative of octahedral coordination as opposed to tetrahedral coordination which results in a strong pre-edge intensity.[20] The two peaks (in the pre-edge region) for Mn are discernable, as Mn is in the tetravalent state (Mn^{4+}), and a single peak structure in the pre-edge region is characteristic of trivalent (Mn^{3+}) Mn compounds. The latter single peak characteristic for trivalent manganese systems can be interpreted as splitting of the t_{2g} and e_g energy levels modified by the Jahn-Teller distortion, though this is not observed in the studied system.[21]

For the Co pre-edge (Fig. 3b), the Co 1s→3d transitions, are not well structured here, but two peaks (C and C') are visible, as well as a weak feature (C and C') above x = 0.31 with indication of an energy splitting in between. C and C' are assigned to the 1s→t_{2g} transition, which is dipole and symmetry forbidden, but occurs, albeit very weakly, due to the mixing with the oxygen p orbitals and quadrupole transitions and 1s→e_g transition which is dipole forbidden, and hence much weaker than the symmetry- and dipole-allowed 1s→4p main transition. The two transitions present here indicate at least a partial high-spin configuration, since the peaks are not clearly split, which may be due to the delocalized electrons in the band structure or an overlapping mixture of low-spin $^1A_1(t_{2g}^6 e_g^0)$, intermediate $^3T_1(t_{2g}^5 e_g^1)$, and high-spin $^5T_3(t_{2g}^4 e_g^2)$ states. The shoulder (B) around 7723 eV is the shake-down process, which occurs at a lower energy since the binding energy decreases due to the core-hole screening effect in Co by an electron transferred in from the ligand.[22, 23]

Since the intensity of the pre-edge peak (1s→3d) can be used as an indicator for the geometry of octahedral complexes, the presence of very weak Ni pre-edge during the cycling signifies that Ni atoms are not highly symmetrical, and the weak pre-edge arises due to the possible distortion of the octahedral **3b** site in the rhombohedral R-3m space group, which results in the removal of the inversion symmetry.

Fig. 4 is a quantitative picture of how the redox process progresses. It shows a plot of the relative white line peak position as a function of amount of Li present (x), in contrast to the edge position, as defined by the energy at half of the edge step for the K edge, observed during charge and discharge. The Co and the Ni peak positions change by +2.2 and +3.7 eV, respectively, as the lithium content changes from the fully discharged state to the charged (4.7 V vs Li) state. Though there is still a controversy regarding charge compensation via oxygen in these systems, the results here show clearly the contribution of the Ni and the Co ions to the charge compensation process, but it is important to note that the smaller shift in the Co edge observed here compared to Ni, can be attributed to the possibility of formation of more covalent bonds of Co with O.

The local structure of the Mn, Co, and Ni atoms in the system was obtained from EXAFS measurements. The backgrounds were subtracted by extrapolating a Victoreen-type function from the pre-edge region, and EXAFS oscillations $\chi(k)$ were extracted using cubic spline baseline functions. In all cases, the Li contribution to the EXAFS was ignored because of the low backscattering ability of the lithium. The FT (Fourier transform) of the data at selected SOC's is shown in Figures 5-7. The first peak (~ 1.5 Å, labeled S) in the FT is attributed to the M(metal)-O interactions while the second peak (~ 2.5 Å labeled T) is due to the M-M interactions. During the cycling process the Mn–O

distances remain nearly unchanged, in contrast to the gradual dwindling of the Co–O distances accompanied by decreases in the Ni–O distances (Fig. 8). This change can be related to the change in the valence state in the transition metals where in an octahedral crystal field, the d-orbitals split into triply degenerate (t_{2g}) and a higher-energy doubly degenerate orbital set (e_g), which leads to an outermost electronic configuration for Co^{3+}/Co^{4+} as $t_{2g}^6e_g^0$ /$t_{2g}^5e_g^0$. On the other hand the outermost configuration for $Ni^{2+}/Ni^{3+}/Ni^{4+}$ can be represented as $t_{2g}^6e_g^2$/ $t_{2g}^6e_g^1$/$t_{2g}^6e_g^0$. Hence during the oxidation reaction of the charging cycle, the energy change for Ni^{2+}/Ni^{4+} (or Ni^{3+}/Ni^{4+}) would be larger (than for Co) as the change takes place between the lower t_{2g} and the higher e_g sets, inducing a larger change in ionic radius from Ni^{2+} to Ni^{4+}(R_{Ni}^{2+} ~0.69 Å/R_{Ni}^{3+} ~0.56 Å/R_{Ni}^{4+} ~0.48 Å). From Figures 6 and 7, it can be seen that the amplitude of the Co-O peak remains almost unchanged while the Ni-O peak increases during charging. These observations can best be explained if we consider the simpler systems of $Li_{1-x}NiO_2$ and $Li_{1-x}CoO_2$. For $LiNiO_2$ studied earlier[24], Ni is surrounded by oxygen atoms at two different distances and the distortion of the octahedral coordination is consistent with the presence of the Jahn-Teller effect due to the Ni^{3+} in the low spin state (in addition to the distortion inherent in R-3m symmetry). On delithiation of $Li_{1-x}NiO_2$, the increase of the Ni-O peak amplitude is ascribed to the change in the oxidation from Ni^{3+} to Ni^{4+} and since Ni^{4+} is not a Jahn-Teller active ion the gradual change of Ni^{3+} to Ni^{4+} during charging diminishes the effect of the Jahn-Teller distortion and results in an increased amplitude of the Ni-O peak. Here in this system based on the above observation we can explain, during delithiation from x = 0.55 to x = 0.19 (when Ni is oxidized from Ni^{3+} to Ni^{4+}) a diminution of the Jahn-Teller effect results in increased amplitude of the Ni–O

peak. On the contrary from x = 1.0 to x = 0.55 (when Ni is oxidized from Ni^{2+} to Ni^{3+}) increase of the Jahn-Teller effect results in a decrease of amplitude of the Ni–O peak. For the $Li_{1-x}CoO_2$ delithiation there is no change in the amplitude of the Co-O peak due to the absence of the Jahn Teller effect for Co^{3+}. Thus similarly for this system, during charging Co changes from Co^{3+} to Co^{4+} neither of which are Jahn Teller active ions, and thus a change in amplitude of the Co-O peak is not observed.

Structural parameters of the Mn, Co, and Ni absorbers were analyzed based on a two shell model, where bond distances (R) and the Debye-Waller factors (σ^2) were left as free parameters, and the coordination number (CN) for Mn–O, Co–O, Ni–O, was kept fixed to the crystallographic value of six (Fig. 8). During cycling, the change in the Ni-O bond length is the largest (~ 0.16Å), followed by Co-O (~ 0.03 Å) and the Mn-O change is negligible (~ 0.006 Å). The Ni-O bondlength at the start of charge (Ni^{2+}) is 2.03 Å, while at x = 0.55 (Ni^{3+}) it is 1.93 Å and finally at x = 0.19 (Ni^{4+}) its 1.88 Å. These Ni-O distances are consistent with octahedrally coordinated systems where the Ni^{2+}–O bond length is about 2.06 Å, Ni^{3+} exhibiting a static Jahn-Teller distortion shows an average Ni^{3+}–O bond at 1.97 Å, finally the Ni^{4+}–O bond length is 1.88 Å.[25-29] Thus these fit results confirm that the average oxidation state of Ni ion at the start of the charge is Ni^{2+}, whereas at x = 0.55 it is Ni^{3+} and finally at the end of the charge Ni ion is close to Ni^{4+}. The significant change in the Ni–O bond length can be explained by the change in oxidation state of Ni^{2+}–Ni^{4+} since the ionic radius of Ni^{2+} (0.69 Å) is larger than that of Ni^{4+} (0.46 Å). For Co, during charging, the observed changes in the Co-O distance (~0.03Å) are attributed to the oxidation of Co^{3+} to Co^{4+}, and the predicted decrease in Co-O distance between Co^{3+} and Co^{4+} is ~0.06-0.08 A.[29] Using reference 30, it can be

estimated that between ~40-50% of the Co is oxidized during the charging cycle. Finally, for the metal-metal (Mn-M, Co-M and Ni-M) interactions fits, we have taken two approaches. In one approach, we have fitted the experimental profile taking Co as the scatterer, (Fig. 9) but because this scattering atom can either be, Mn, Co, or Ni (though not Al because it is too light) we also did fits with the Mn and Ni atoms. This was done to understand the sensitivity of the data taking Co as the scatterer. In this approach we found that if instead of Co, it was fitted with Ni or Mn the corresponding bond distances shown in Fig. 9 during the cycling changes by +0.01 Å for Ni and -0.01 Å for Mn. In the other approach, which actually gives similar result as shown in Fig. 9, we fitted the M-M peak by taking into consideration the ratio of Mn, Co and Ni present initial at the beginning of the charging cycle.

Conclusions

In-situ XAS characterizations for Al-substituted $Li(Ni_{0.4}Co_{0.15}Al_{0.05}Mn_{0.4})O_2$ have been performed during the first charge and discharge process, providing us with an excellent tool for analyzing the changes that occur when Li is cycled in and out of the layered lattice. During cycling, Mn is electrochemically inactive and remains tetravalent (Mn^{4+}), whereas divalent nickel (Ni^{2+}) is oxidized mostly to tetravalent nickel (Ni^{4+}), passing through an intermediate stage of trivalent nickel (Ni^{3+}), and about ~40-50% of Co^{3+} is converted to Co^{4+} during charge. With the doping of Al, there are only small volumetric changes in the system compared to the parent material, and the system retains its hexagonal lattice structure, and electrochemical properties, confirming that this material possesses very desirable characteristics for an electrode, in keeping with the goal

of reducing the amount of Co in the electrode for use in Li-ion intercalation cell applications.

Acknowledgements:

Work was performed at the DND-CAT beam line, which is supported by the E. I. DuPont de Nemours and Co., the Dow Chemical Company, the U.S. National Science Foundation through grant no. DMR-9304725, and the State of Illinois through the Department of Commerce and the Board of Higher Education grant no. IBHE HECA NWU 96. This work was supported by the Assistant Secretary for Energy Efficiency and Renewable Energy, Office of Vehicle Technologies of the U.S. Department of Energy under Contract No. DE-AC02-05CH11231.

Table I:

Electrode Properties and Experimental Conditions

$Li(Ni_{0.4}Co_{0.15}Al_{0.05}Mn_{0.4})O_2$	Formula weight: 94.5815
Ni^{+2} to Ni^{+4} specific capacity	226.694 mAh/g
Co^{+3} to Co^{+4} specific capacity	42.505 mAh/g
Total specific capacity	269.199 mAh/g
Active material weight	14.7 mg
Electrode area	1.77 cm^2
Active material loading	8.31 mg/cm^2
Total current	0.18 mA

Figure Captions:

Figure 1:

Charging curve of the $Li_x(Ni_{0.4}Co_{0.15}Al_{0.05}Mn_{0.4})O_2$ electrode. Labels shown A to O are the points where the measurements were performed during the charging cycle corresponding to x = 1.0 (A), 0.96 (B), 0.92 (C), 0.88 (D), 0.84 (E), 0.80 (F), 0.76 (G), 0.67 (H), 0.55 (I), 0.49 (J), 0.38 (K), 0.31 (L), 0.27 (M), 0.23 (N) and 0.19 (O).

Figure 2:

Normalized XANES comparison for $Li(Ni_{0.4}Co_{0.15}Al_{0.05}Mn_{0.4})O_2$ of (a) Mn K edge at x = 1.0 with the model compound Mn_2O_3 (Mn^{3+}) and MnO_2 (Mn^{4+}); (b) Co K edge observed at x = 1.0 with the model compound $LiCoO_2$ (Co^{3+}), and (c) Ni K edge for at x =1.0 and x = 0.55 with the model compounds nickel (II) oxide (Ni^{2+}) and $LiNi_{0.8}Co_{0.2}O_2$ (Ni^{3+}), respectively.

Figure 3:

Normalized XANES spectra at different states of charge of (a) Mn K edge, (b) Co K edge, and (c) Ni K edge, respectively. The insets show the nature of the pre-edge peaks of the respective XAS spectra; (d) Comparison of the linear combination (LC) best fit of the Ni^{2+} (x =1.0) and Ni^{4+} (x = 0.19) spectra (with a composition of 62%, of x =1.0 and 38%, of x = 0.19) with the x = 0.55 (Ni^{3+}) spectra.

Figure 4:

Plot of the white line energy shift vs the x in $Li_x(Ni_{0.4}Co_{0.15}Al_{0.05}Mn_{0.4})O_2$, for the Ni K edge. The filled symbol (•) represents the data during the charge, while the empty symbol (o) represents the data during discharge.

Figure 5:

Mn-K edge k^3-weighted Fourier transform at selected Li content (x) during the charge cycle (k range = 1.5–15.5 $Å^{-1}$). M represents the transition metal atom.

Figure 6:

Co-K edge k^3-weighted Fourier transform at selected Li content (x) during the charge cycle (k range = 1.5–12.5 $Å^{-1}$). M represents the transition metal atom.

Figure 7:

Ni-K edge k^3-weighted Fourier transform at selected Li content (x) during the charge cycle (k range = 1.5–15.5 $Å^{-1}$). M represents the transition metal atom.

Figure 8:

Metal-oxygen first shell coordination bond length changes during Li/ $Li_x(Ni_{0.4}Co_{0.15}Al_{0.05}Mn_{0.4})O_2$ cell cycling. x = 1.0 to 0.19 represent first charging cycle and x = 0.19 to 1.0 represent first discharge cycle.

Figure 9:

Metal-metal first shell coordination bond length changes during Li/ $Li(Ni_{0.4}Co_{0.15}Al_{0.05}Mn_{0.4})O_2$ cell cycling. x = 1.0 to 0.19 represent first charging cycle and x = 0.19 to 1.0 represent first discharge cycle.

References:

[1] T. Ohzuku, A. Ueda, and M. Nagayama, Solid State Ionics 67, 123 (1993)

[2] G. Amtucci, A. Du Pasquier, A. Blyr, T. Zheng, and J. M. Tarascon, Electrochim. Acta 45, 255 (1999); C. H. Chen, J Liu, M.E. Stoll, G. Henriksen, D.R. Vissers, and K. Amine, J. Power Sources, 128, 278 (2004)

[3] X. Zang P. N. Ross, Jr., R. Kostecki, F. Kong, S. Sloop, J. B. Kerr, K. Striebel, E. J. Cairns, and F. McLarnon, J. Electrochem. Soc., 148, A463 (2001); N. Yabuuchi, Y. Makimura, and T. Ohzuku, J. Electrochem. Soc., 154, A314 (2007)

[4] J. K. Ngala, N.A. Chernova, M. Ma. M. Mamak, P.Y. Zavalij and M. S. Whittingham, J. Mater. Chem., 14, 214 (2004); T. Ohzuku and Y. Makimura, Chem. Lett. 30, 642 (2001)

[5] K. M. Shaju, G. V. Subba Rao, and B. V. R. Chowdari, Electrochim. Acta 48, 145 (2002)

[6] Z. Lu, D. D. MacNeil, and J. R. Dahn, Electrochem. Solid-State Lett. 4, A200 (2001)

[7] D. D. MacNeil, Z. Lu, and J. R. Dahn, J. Electrochem. Soc. 149, A1332 (2002)

[8] J. Wilcox, S. Patoux, and M. Doeff, J. Electrochem. Soc., 156, A192 (2009)

[9] James D. Wilcox, Efrain E. Rodrigue and Marca M. Doeff, J. Electrochem. Soc., 156, A1011 (2009)

[10] F. Zhou, X. Zhao, Z. Lu, J. Jiang, and J. R. Dahn, Electrochem. Solid-State Lett., 11, A155 (2008)

[11] F. Zhou, X. Zhao, Z. Lu, J. Jiang, and J. R. Dahn, Electrochem. Commun., 10, 1168 (2008)

[12] A. Deb, U. Bergmann, E. J. Cairns, and S. P. Cramer, J. Synchrotron Radiat., 11, 497 (2004)

[13] G. N. George and I. J. Pickering, Exafspak, Stanford Synchrotron Radiation Laboratory, Stanford, CA, (1993)

[14] M. Newville, J. Synchrotron Radiat., 8, 322 (2001)

[15] Y. Koyama, I. Tanaka, H. Adachi, Y. Makimura, and T. Ohzuku, J. Power Sources, 119–121, 644 (2003)

[16] S. Sugano, Y. Tanabe, and H. Kamimura, Multiplets of Transition-Metal Ions, Vol. 1, p. 73, Academic, New York (1970)

[17] J. S. Griffith, The Theory of Transition Metal Ions, Cambridge University Press, Cambridge, England (1961)

[18] A. Manceau, A. I. Gorshkov, and V. A. Drits, Am. Mineral., 77, 1133 (1992); B. Poumellec, V. Kraizman, Y. Aifa, R. Cortes, A. Novakovich, and R. Vedrinskii, Phys. Rev. B, 58, 6133 (1998); O. Sipr, A. Simunek, S. Bocharov, T. Kirchner, and G. Drager, Phys. Rev. B, 60, 14115 (1999)

[19] James. E. Hahn, R. A. Scott, K. O. Hodgson, S. Doniach, S. R. Desjardins, and E. I. Solomon, Chem. Phys. Lett., 88, 595 (1982)

[20] M. Belli, A. Scafati, A. Bianconi, S. Mobilio, L. Palladino, A. Reale, and E. Burattini, Solid State Commun. 35, 355 (1980); A. Manceau, A. I. Gorshkov, and V. A. Drits, Am. Mineral. 77, 1133 (1992)

[21] C. R. Horne, U. Bergmann, M. M. Grush, R. C. C. Perera, D. L. Ederer, T. A. Callcott, E. J. Cairns, and S. P. Cramer, J. Phys. Chem. B 104, 9587 (2000)

[22] Y. Iwasawa, X-Ray Absorption Fine Structure for Catalyst and Surfaces, World Scientific, Singapore (1996)

[23] A. Chainani, M. Mathew, and D. D. Sharma, Phys. Rev. B 46, 9976 (1992)

[24] A. Rougier, C. Delmas, and A. V. Chadwick, Solid State Commun., 94, 123 (1995)

[25] T. W. Capehart, D. A. Corrigan, R. S. Conell, K. I. Pandya, and R. W. Hoffman, Appl. Phys. Lett. 58, 865 (1991)

[26] A. N. Mansour and C. A. Melendres, J. Phys. Chem. A 102, 65 (1998)

[27] W. E. O'Grady, K. I. Pandya, K. E. Swider, and D. A. Corrigan, J. Electrochem. Soc. 143, 1613 (1996)

[28] A. N. Mansour, J. McBreen, and C. A. Melendres, J. Electrochem. Soc. 146, 2799 (1999)

[29] R. D. Shannon, Acta Crystallogr., Sect. A: Cryst. Phys., Diffr., Theor. Gen. Crystallogr. 32, 751 (1976)

[30] I. D. Brown and D. Altermatt, Acta Cryst. B41, 244-247 (1985)

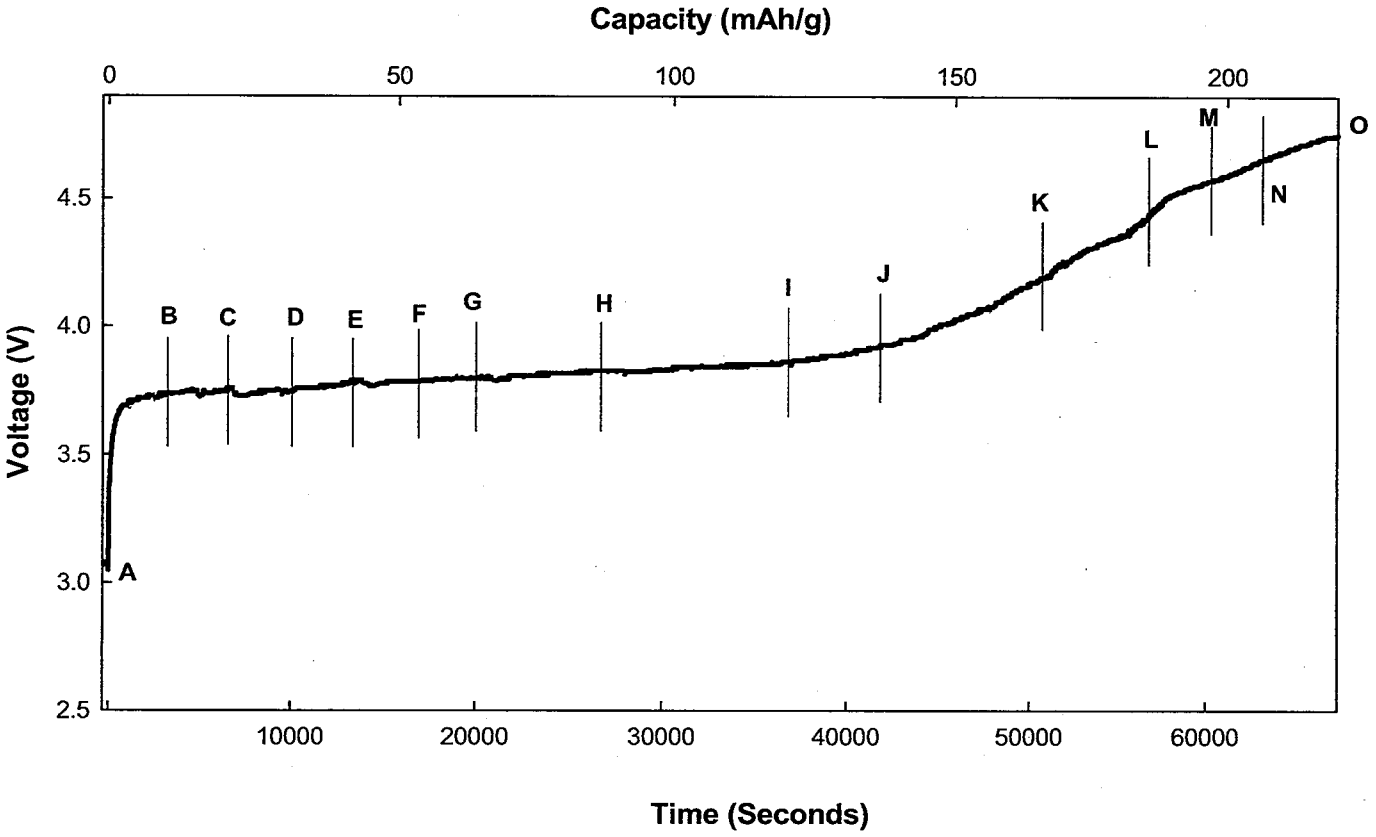
Capacity (mAh/g)
0
50
100
150
200
Voltage (V)
4.5
4.0
3.5
3.0
2.5
A
B
C
D
E
F
G
H
I
J
K
L
M
N
O
10000
20000
30000
40000
50000
60000
Time (Seconds)

Figure 1

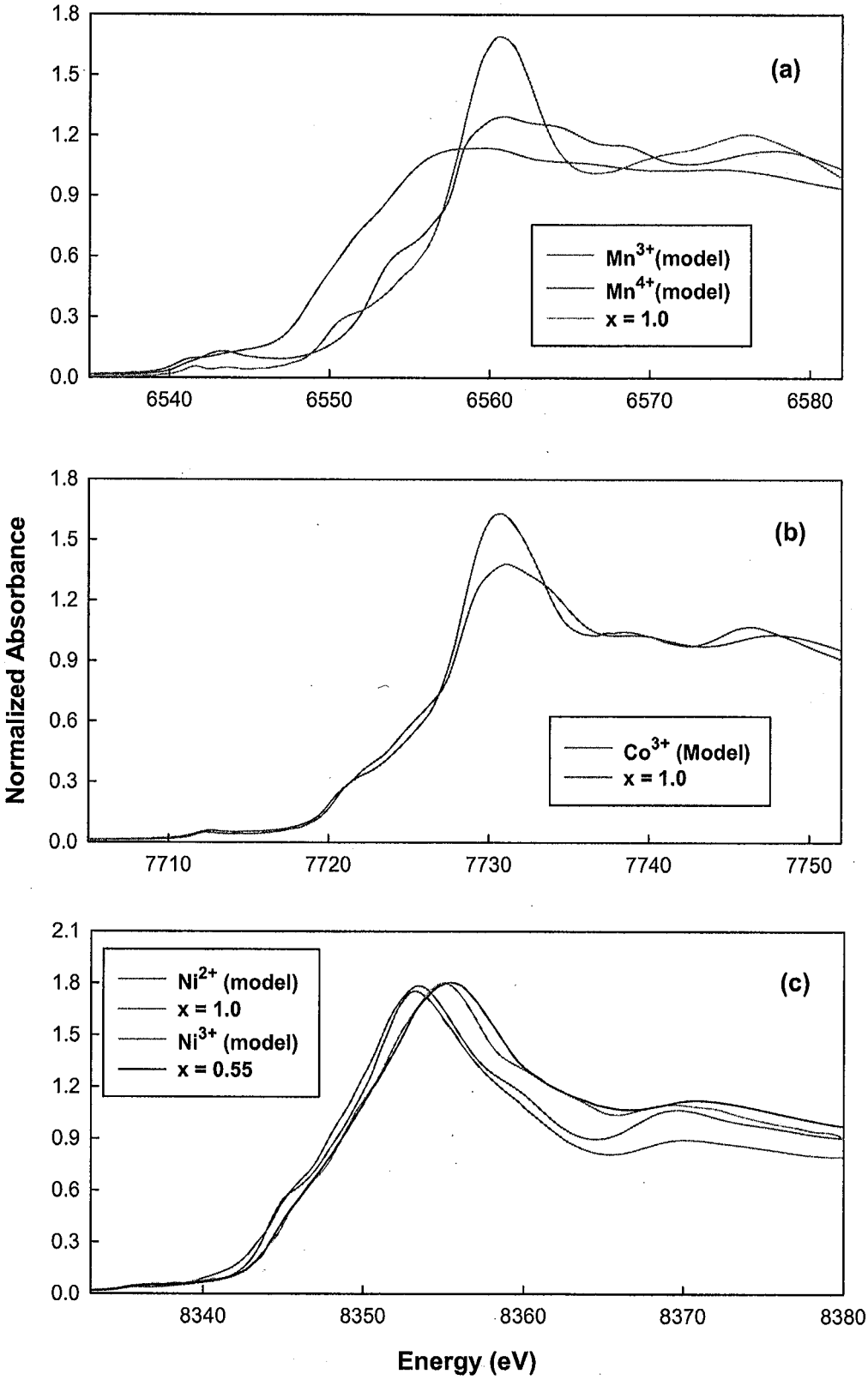
(a)
Mn3+(model)
Mn4+(model)
x = 1.0
(b)
Co3+ (Model)
x = 1.0
(c)
Ni2+ (model)
x = 1.0
Ni3+ (model)
x = 0.55
Normalized Absorbance
Energy (eV)

Figure 2

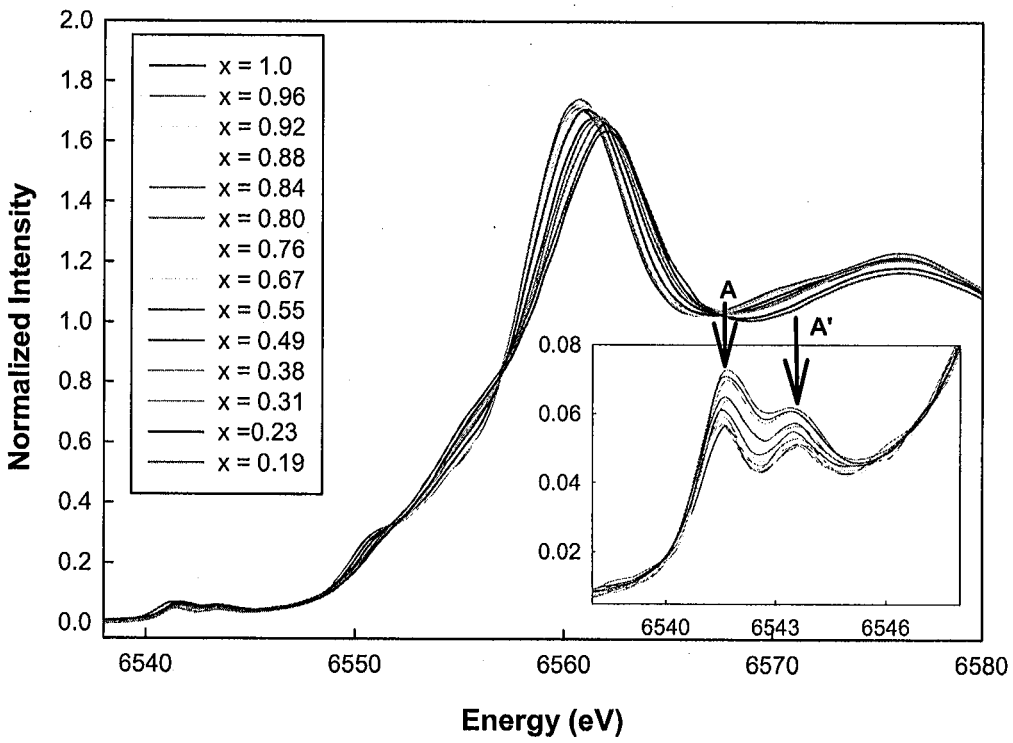
Normalized Intensity
Energy (eV)
x = 1.0
x = 0.96
x = 0.92
x = 0.88
x = 0.84
x = 0.80
x = 0.76
x = 0.67
x = 0.55
x = 0.49
x = 0.38
x = 0.31
x =0.23
x = 0.19
A
A'
2.0
1.8
1.6
1.4
1.2
1.0
0.8
0.6
0.4
0.2
0.0
6540
6550
6560
6570
6580
0.08
0.06
0.04
0.02
6540
6543
6546

Figure 3(a)

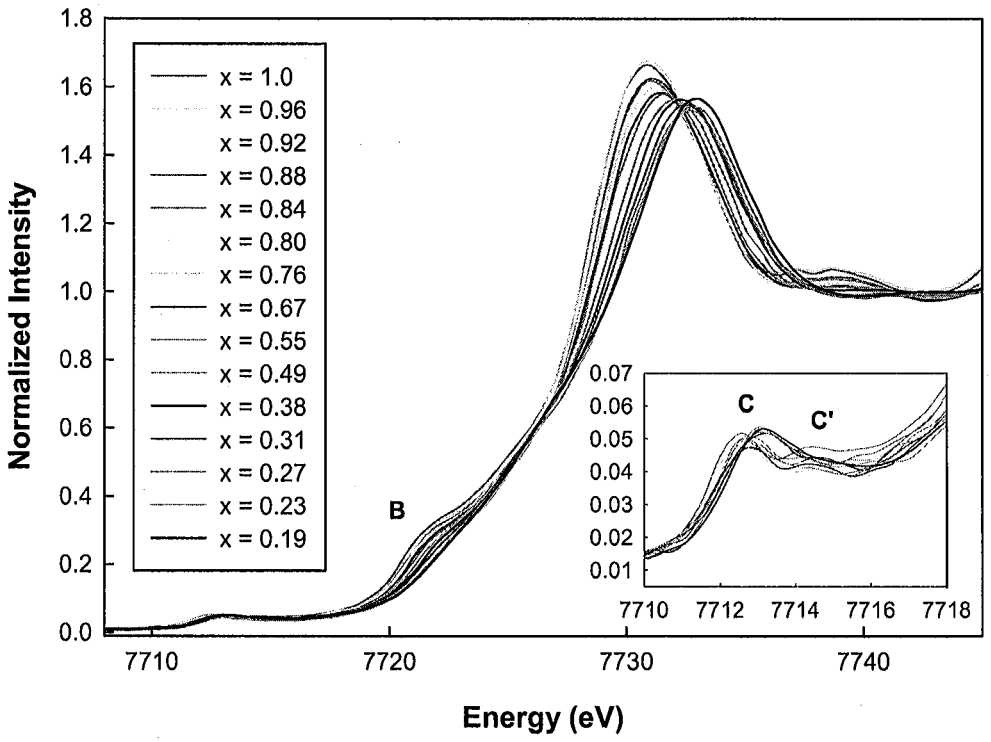
Normalized Intensity
Energy (eV)
x = 1.0
x = 0.96
x = 0.92
x = 0.88
x = 0.84
x = 0.80
x = 0.76
x = 0.67
x = 0.55
x = 0.49
x = 0.38
x = 0.31
x = 0.27
x = 0.23
x = 0.19
B
C
C'

Figure 3(b)

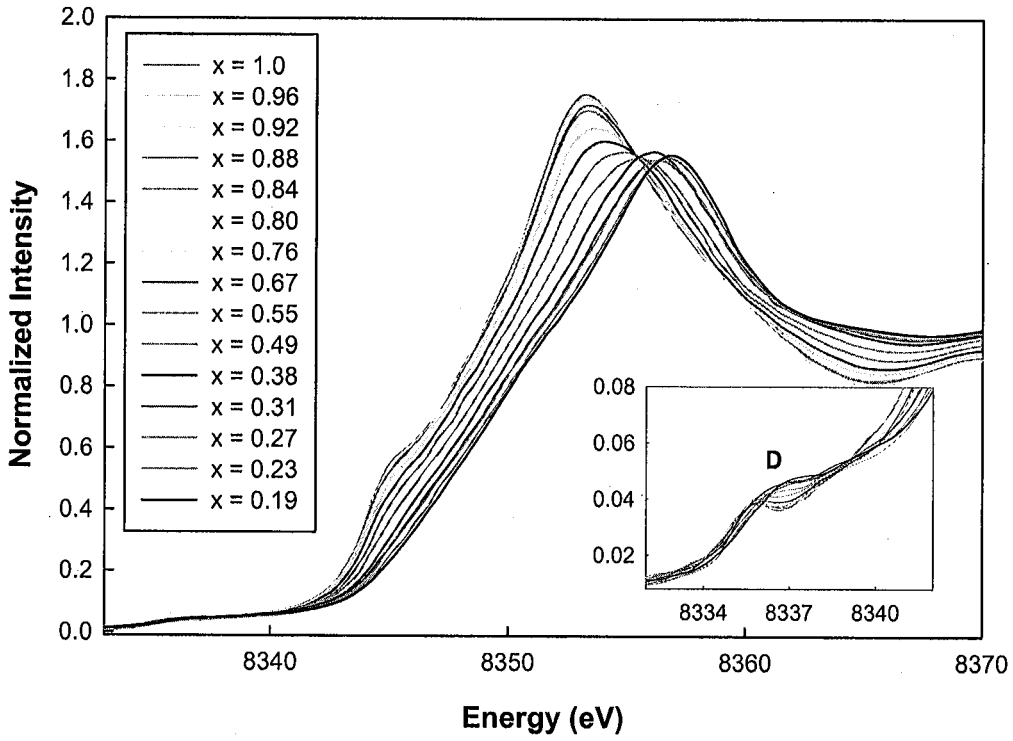
Normalized Intensity
Energy (eV)
x = 1.0
x = 0.96
x = 0.92
x = 0.88
x = 0.84
x = 0.80
x = 0.76
x = 0.67
x = 0.55
x = 0.49
x = 0.38
x = 0.31
x = 0.27
x = 0.23
x = 0.19
D
0.0
0.2
0.4
0.6
0.8
1.0
1.2
1.4
1.6
1.8
2.0
8340
8350
8360
8370
0.02
0.04
0.06
0.08
8334
8337
8340

Figure 3(c)

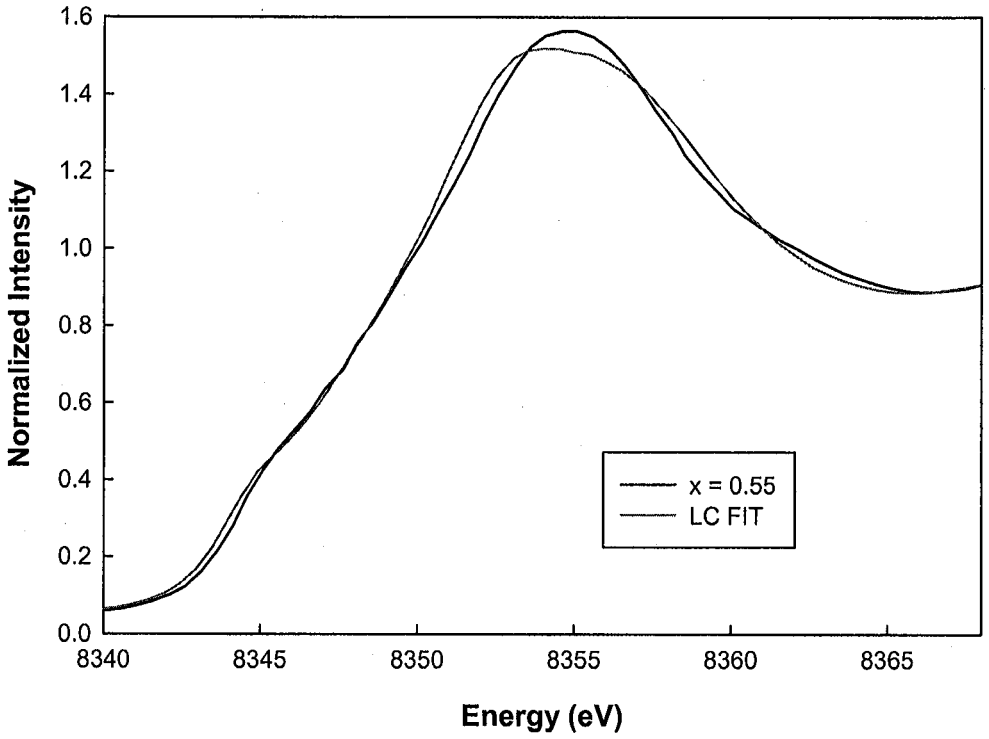
Normalized Intensity
1.6
1.4
1.2
1.0
0.8
0.6
0.4
0.2
0.0
8340
8345
8350
8355
8360
8365
Energy (eV)
x = 0.55
LC FIT

Figure 3(d)

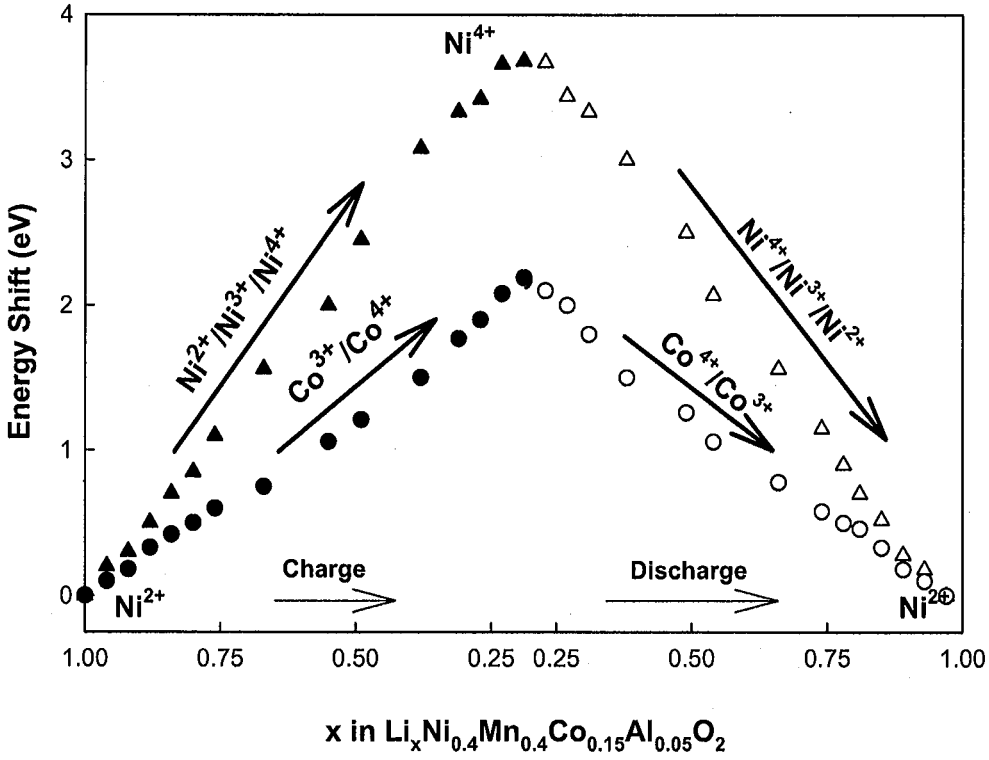
Energy Shift (eV)
4
3
2
1
0
Ni4+
Ni2+/Ni3+/Ni4+
Co3+/Co4+
Ni4+/Ni3+/Ni2+
Co4+/Co3+
Charge
Discharge
Ni2+
Ni2+
1.00
0.75
0.50
0.25
0.25
0.50
0.75
1.00
x in LixNi0.4Mn0.4Co0.15Al0.05O2

Figure 4

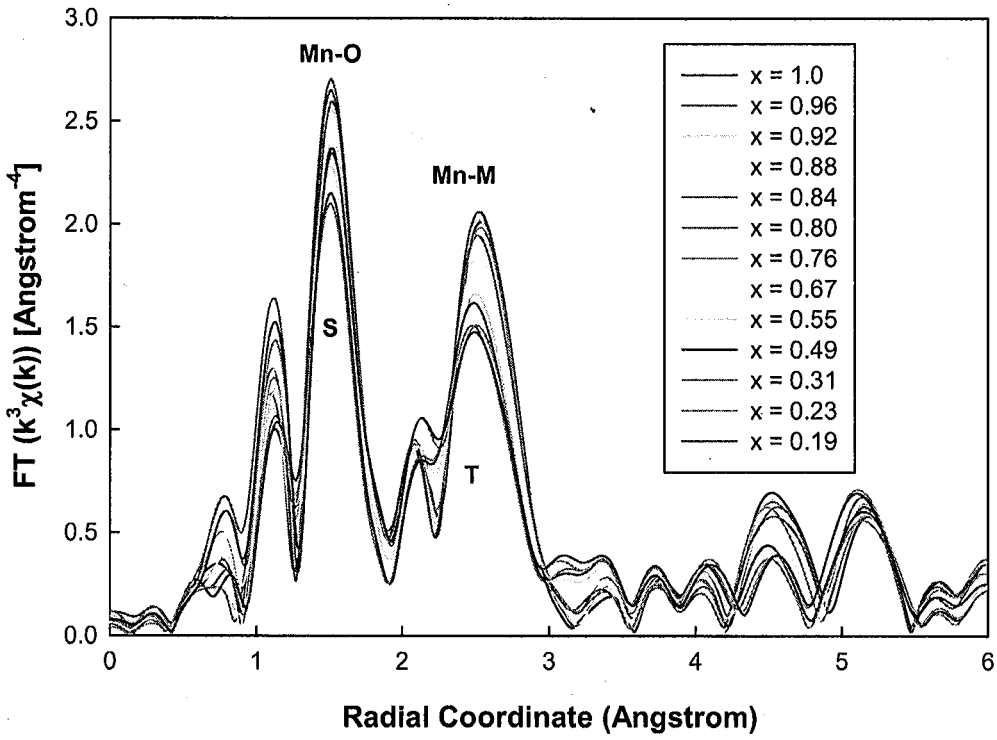
Mn-O
Mn-M
S
T
x = 1.0
x = 0.96
x = 0.92
x = 0.88
x = 0.84
x = 0.80
x = 0.76
x = 0.67
x = 0.55
x = 0.49
x = 0.31
x = 0.23
x = 0.19
FT (k3χ(k)) [Angstrom-4]
Radial Coordinate (Angstrom)
0.0
0.5
1.0
1.5
2.0
2.5
3.0
0
1
2
3
4
5
6

Figure 5

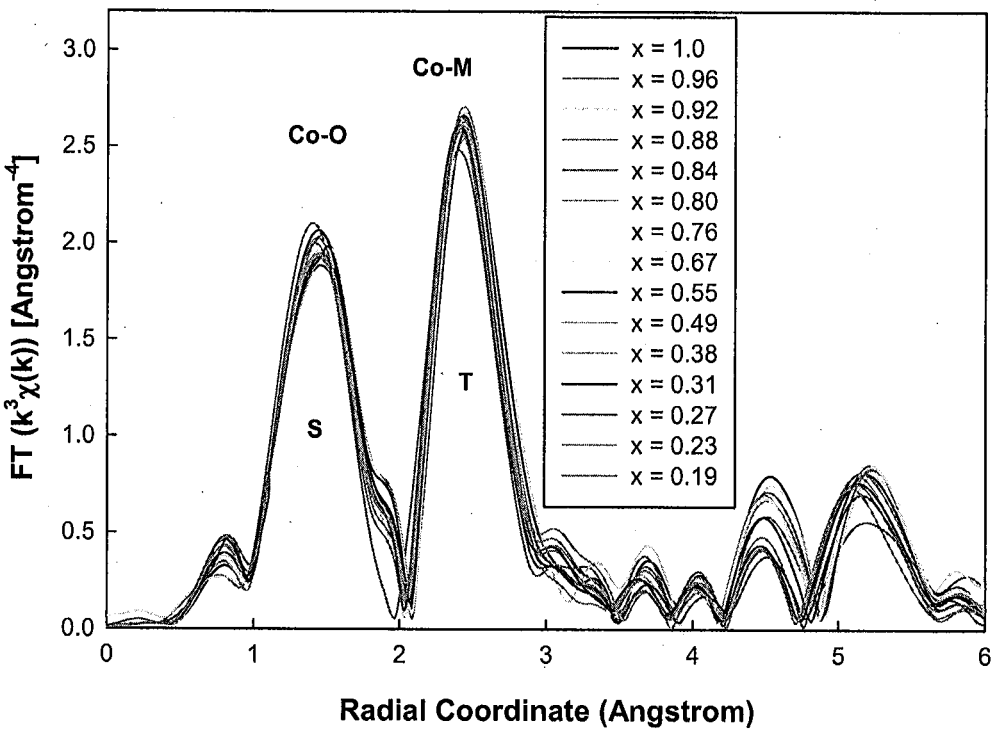
Co-O
Co-M
S
T
x = 1.0
x = 0.96
x = 0.92
x = 0.88
x = 0.84
x = 0.80
x = 0.76
x = 0.67
x = 0.55
x = 0.49
x = 0.38
x = 0.31
x = 0.27
x = 0.23
x = 0.19
FT (k3χ(k)) [Angstrom-4]
Radial Coordinate (Angstrom)
0.0
0.5
1.0
1.5
2.0
2.5
3.0
0
1
2
3
4
5
6

Figure 6

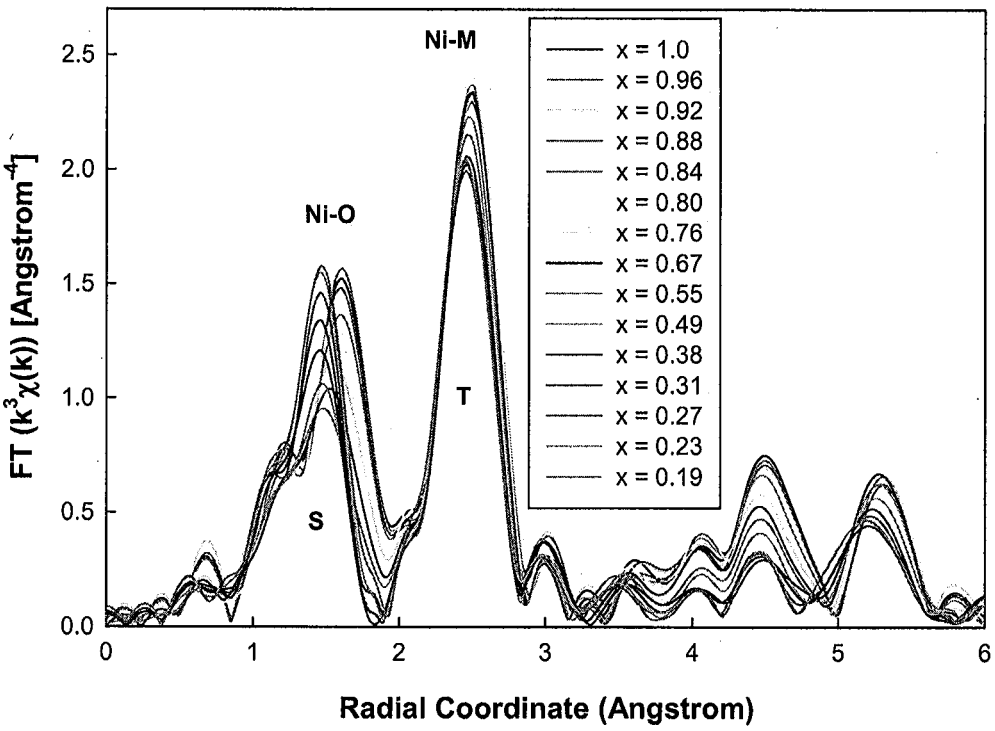
Ni-M
Ni-O
T
S
x = 1.0
x = 0.96
x = 0.92
x = 0.88
x = 0.84
x = 0.80
x = 0.76
x = 0.67
x = 0.55
x = 0.49
x = 0.38
x = 0.31
x = 0.27
x = 0.23
x = 0.19
FT (k3χ(k)) [Angstrom-4]
Radial Coordinate (Angstrom)
0.0
0.5
1.0
1.5
2.0
2.5
0
1
2
3
4
5
6

Figure 7

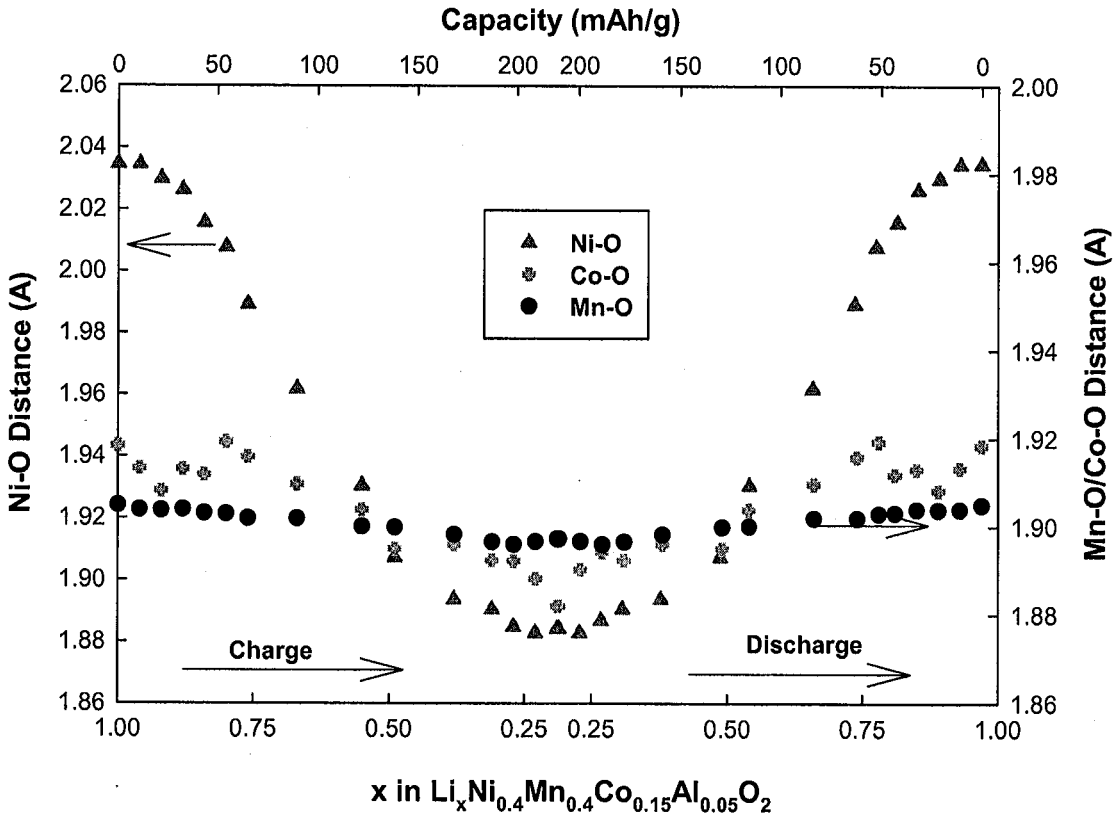
Capacity (mAh/g)
0 50 100 150 200 200 150 100 50 0
Ni-O Distance (A)
Mn-O/Co-O Distance (A)
2.06 2.04 2.02 2.00 1.98 1.96 1.94 1.92 1.90 1.88 1.86
2.00 1.98 1.96 1.94 1.92 1.90 1.88 1.86
Ni-O
Co-O
Mn-O
Charge
Discharge
1.00 0.75 0.50 0.25 0.25 0.50 0.75 1.00
x in $Li_xNi_{0.4}Mn_{0.4}Co_{0.15}Al_{0.05}O_2$

Figure 8

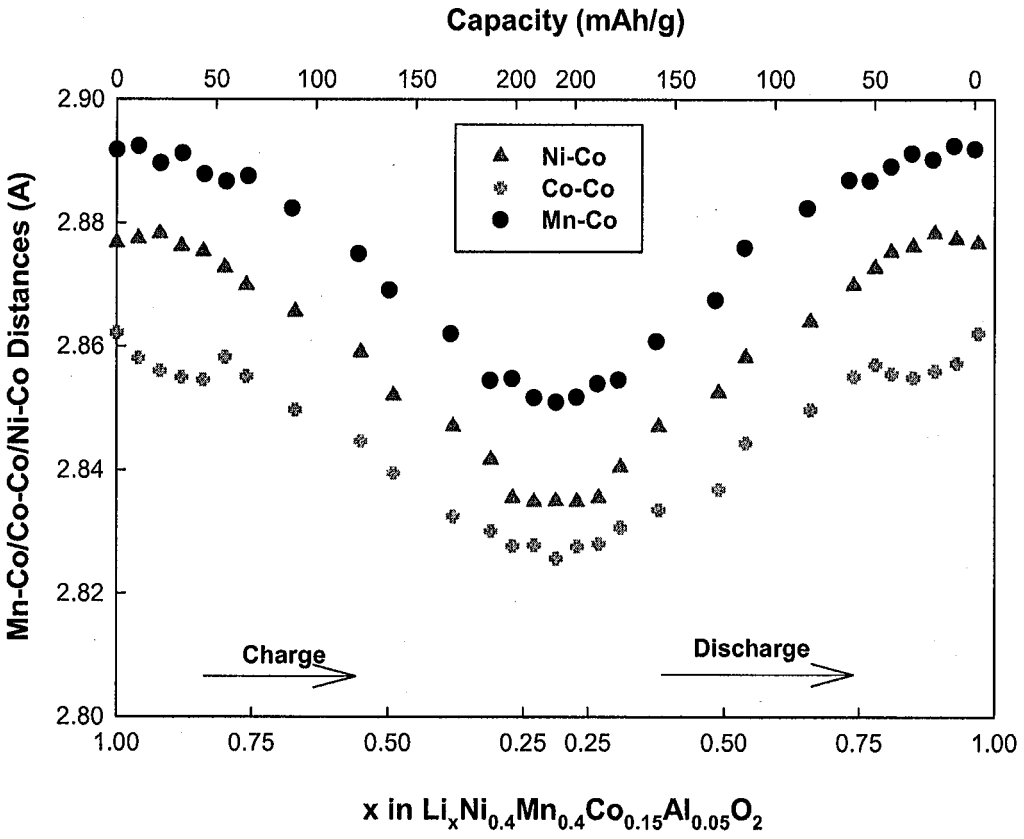
Capacity (mAh/g)
0
50
100
150
200
200
150
100
50
0
2.90
2.88
2.86
2.84
2.82
2.80
Mn-Co/Co-Co/Ni-Co Distances (A)
Ni-Co
Co-Co
Mn-Co
Charge
Discharge
1.00
0.75
0.50
0.25
0.25
0.50
0.75
1.00
x in $Li_xNi_{0.4}Mn_{0.4}Co_{0.15}Al_{0.05}O_2$

Figure 9